

High pressure study of B12As₂: Electrical transport behavior and the role of grain boundaries

Qinglin Wang, Cailong Liu, Boheng Ma, Yang Gao, Matthew Fitzpatrick, Yuqiang Li, Bao Liu, Chunxiao Gao, and Yanzhang Ma

Citation: *Journal of Applied Physics* **117**, 045302 (2015); doi: 10.1063/1.4906462

View online: <http://dx.doi.org/10.1063/1.4906462>

View Table of Contents: <http://scitation.aip.org/content/aip/journal/jap/117/4?ver=pdfcov>

Published by the AIP Publishing

Articles you may be interested in

[Photoluminescence investigation of the indirect band gap and shallow impurities in icosahedral B12As₂](#)
J. Appl. Phys. **112**, 013508 (2012); 10.1063/1.4729920

[On the role of grain boundaries in nanocrystalline \$\gamma\$ -Fe₂O₃ under high pressure](#)
J. Appl. Phys. **111**, 063718 (2012); 10.1063/1.3695459

[Grain boundary effect on the \$\beta\$ -boron electrical transport properties at high pressure](#)
Appl. Phys. Lett. **97**, 174101 (2010); 10.1063/1.3505751

[Novel technique to control oxygen fugacity during high-pressure measurements of grain boundary conductivities of rocks](#)
Rev. Sci. Instrum. **80**, 033903 (2009); 10.1063/1.3097882

[In situ electrical impedance spectroscopy under high pressure on diamond anvil cell](#)
Appl. Phys. Lett. **91**, 092124 (2007); 10.1063/1.2778760



AIP | **Journal of Applied Physics**

Meet The New Deputy Editors



Christian
Brosseau



Laurie
McNeil



Simon
Phillpot

High pressure study of $B_{12}As_2$: Electrical transport behavior and the role of grain boundaries

Qinglin Wang,^{1,2,3} Cailong Liu,² Boheng Ma,⁴ Yang Gao,¹ Matthew Fitzpatrick,¹ Yuqiang Li,¹ Bao Liu,¹ Chunxiao Gao,^{2,a)} and Yanzhang Ma^{1,a)}

¹Department of Mechanical Engineering, Texas Tech University, Lubbock, Texas 79409, USA

²State Key Laboratory of Superhard Materials, Institute of Atomic and Molecular Physics, Jilin University, Changchun 130012, People's Republic of China

³Center for High Pressure Science and Technology Advanced Research, Shanghai 201203, People's Republic of China

⁴Department of Chemical Engineering, University of Maryland, College Park, Maryland 20742, USA

(Received 11 October 2014; accepted 12 January 2015; published online 23 January 2015)

Using a diamond anvil cell, the evolutions of alternate-current impedance spectra and direct-current resistivity in $B_{12}As_2$ have been investigated up to 51.9 GPa. The results provide evidence for the existence of grain and grain boundary effects that are separated in the frequency region. The grain boundary resistance shows a relatively smaller contribution to the total resistance above 16.8 GPa. By using the double-Schottky barrier model, the space charge potential was obtained. A pressure-induced inversion of charge defect concentration in the space charge layer was found at 20.7 GPa. The high-temperature resistivity measurements indicate that the transport activation energy is determined by defect energy levels in the band gap. © 2015 AIP Publishing LLC.

[<http://dx.doi.org/10.1063/1.4906462>]

I. INTRODUCTION

In boron and boron-rich compounds, the majority of boron atoms form a 12-element icosahedra cluster with strong covalent bonds in between as well as with adjacent icosahedra and other structural elements.¹ This unusual structure is believed to account for many unique engineering properties of high hardness, high stability, and high brittleness, in addition to its exceptional semiconductivity and superconductivity.^{2–5} Among many other boron compounds, boron arsenide ($B_{12}As_2$), a wide bandgap semiconductor, has recently become the target of interest for its potential application in avant-garde devices such as beta-voltaic cells and neutron detectors because of its “self-heal” capability under intense ionizing radiation.^{6,7}

$B_{12}As_2$ has a rhombohedral structure with the two arsenate atoms along the body diagonal to link the icosahedra. Raman spectroscopy studies revealed that the $B_{12}As_2$ crystal structure is stable up to 80 GPa before a reversible transition to a distorted structure along with a strong deformation of the icosahedral structure.⁸ High-pressure X-ray diffraction measurement performed up to 25.5 GPa also confirmed the structural stability and determined that the boron icosahedron plays a dominant role in the compressibility of $B_{12}As_2$.⁹ In former studies of conductivity properties, it was found that $B_{12}As_2$ has a relatively high hole mobility that may result in a high current carrying capacity,¹⁰ yet its wide energy bandgap leads to a low intrinsic conductivity at ambient conditions.¹¹ High pressure may lead not only to structural and electronic phase transformations and consequently to changes in the properties accounting for the conductivity of a material, but also to gradual modulation of the bandgap,

charge carrier concentration, and carrier mobility. It may also lead to new phenomena in a material.

Another important aspect of polycrystalline $B_{12}As_2$ is its powdered state. Different from single crystalline, the polycrystalline state has a large number of grain boundaries that bring special properties. Two examples are the plastic deformation and fracture of bicrystals of metals¹² and ceramics.¹³ The activity of the grain boundary strongly depends on the boundary structure and character, and also on the geometric arrangement of the boundary in the sample. Usually, grain boundaries are produced by the interaction between neighboring grains or some other additives, which can improve the original performance of bulk materials or even generate a property that has not found on individual grains.¹⁴ Thus, the interaction of grains across a grain boundary can be the source of desirable bulk properties, if the grain boundary can be properly designed and controlled. It is therefore worthwhile to explore how the grain boundaries, in particular, influence the transport properties of $B_{12}As_2$.

In the present work, we explore the transport properties of polycrystalline $B_{12}As_2$ under high pressure by means of variable-frequency alternate-current impedance spectroscopy in a diamond anvil cell and direct-current (DC) resistivity at high temperatures, with emphasis on the role of the grain boundary on the conduction mechanism.

II. EXPERIMENTAL

In the experiments, we performed delicate micro fabrication processes on the diamond anvil and the gasket in order to construct a proper electrical circuit around the sample to make it possible to precisely perform electrical measurements. In the gasket fabrication, a sheet of T-301 stainless steel was pre-indented to a thickness of 30 μm , on which a

^{a)}Authors to whom correspondence should be addressed. Electronic addresses: cxgao599@aliyun.com and y.ma@ttu.edu

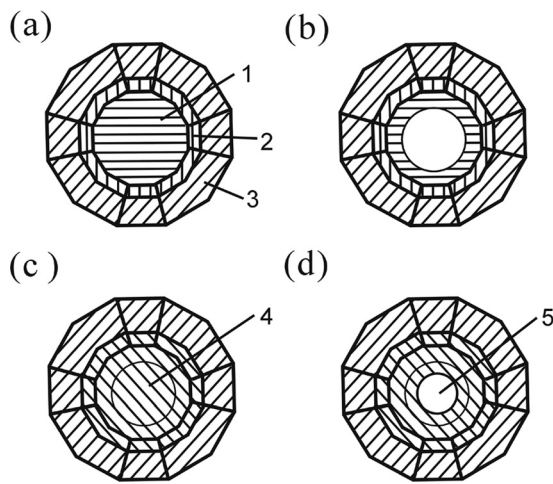


FIG. 1. Manufacturing process and configuration of the insulating gasket. (a) An indentation was made on a steel gasket, (b) a hole was drilled into the indented gasket, (c) the drilled hole was packed with a mixture of diamond powder and epoxy, and (d) a hole was drilled on the compacted mixture. Numbers indicate 1, the diamond flat facet; 2, the small angle bevel; 3, the side faces; 4, the mixture of diamond powder and epoxy; and 5, the sample chamber hole.

hole of $250\text{ }\mu\text{m}$ in diameter was laser drilled. To insulate the gasket from the electrodes on the anvils, the hole was filled and compacted with a mixture of diamond powder and epoxy, on which a smaller hole of $170\text{ }\mu\text{m}$ in diameter was drilled to eventually serve as the sample chamber (Fig. 1).

In the circuit fabrication, a diamond with a culet of $400\text{ }\mu\text{m}$ in diameter was first made chemically clean (Fig. 2(a)). A Mo film was then deposited onto its facet (Fig. 2(b)), which

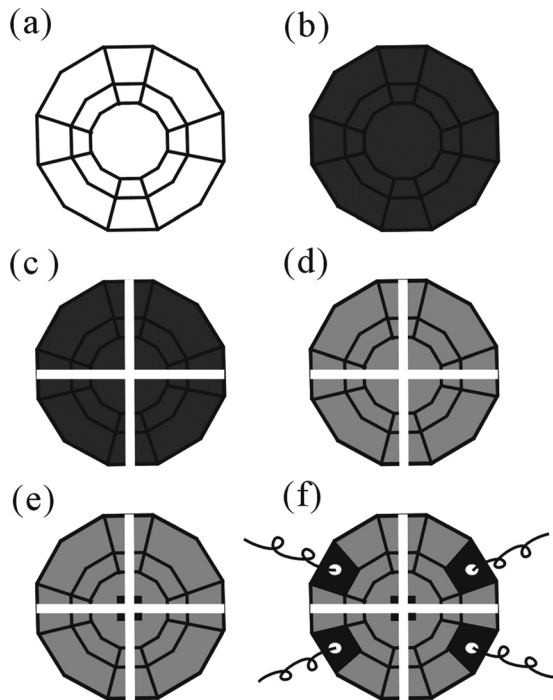


FIG. 2. Manufacturing process and configuration of a microcircuit on a diamond anvil: (a) A clean diamond anvil. (b) A Mo film sputtered on a diamond anvil. (c) A Mo film patterned into four sections. (d) An Al_2O_3 layer sputtered. (e) Part of the Al_2O_3 layer removed to allow required exposure. (f) The configuration of the microcircuit.

was patterned into four sections through a photolithography and chemical etching method (Fig. 2(c)) to serve as conducting electrodes. Then, the entire top of the anvil was sputtered with an Al_2O_3 layer (Fig. 2(d)) to build insulation from the metallic gasket. An area in the center of the Al_2O_3 layer was removed chemically, leaving the electrodes exposed to contact with the sample inside the sample chamber for measurement (Fig. 2(e)). See reference for additional information.¹⁵

The B_{12}As_2 sample was synthesized by precipitation from molten nickel solutions saturated with elemental boron and arsenic.¹⁶ In the sample thickness measurements, the deformation of the diamond was considered to be elastic and the same at a given pressure during loading and unloading. Based on the assumption of completely plastic deformation on the gasket, the actual thickness of the sample (t) at every pressure during the compressing process can be expressed by $t = L_m + \delta_P$, where L_m represents the sample thickness at maximum pressure and δ_P is the thickness difference between loading and unloading at every pressure.¹⁷ The impedance spectroscopy was measured with a Solartron 1260 impedance analyzer equipped with a Solartron 1296 dielectric interface. In the measurements, a 0.1 V sine-signal voltage was applied on the sample with frequencies varying in steps from 0.1 to 10^7 Hz . The temperature dependent resistivity measurements were performed by a Keithley 2400 Source Meter and a Keithley 2700 Multimeter. In the high temperature measurements, the sample in the diamond anvil cell was heated in a tropical drying cabinet and a measurement was performed 10 min after the temperature became stable.¹⁸ The pressure was determined from the pressure-driven shift of the ruby $R1$ fluorescence line.¹⁹ The impedance measurements were performed from 2.8 to 51.9 GPa .

III. RESULTS AND DISCUSSION

The complex impedance spectrum is a powerful tool in separating out the grain and the grain boundary effects. Figure 3 displays some of the Nyquist plots of the impedance spectra of B_{12}As_2 at various pressures. The abscissa axis represents the real part of the impedance Z' , whereas the ordinate axis represents the imaginary part Z'' . Each spectrum is found to consist of two semicircle arcs. The low frequency

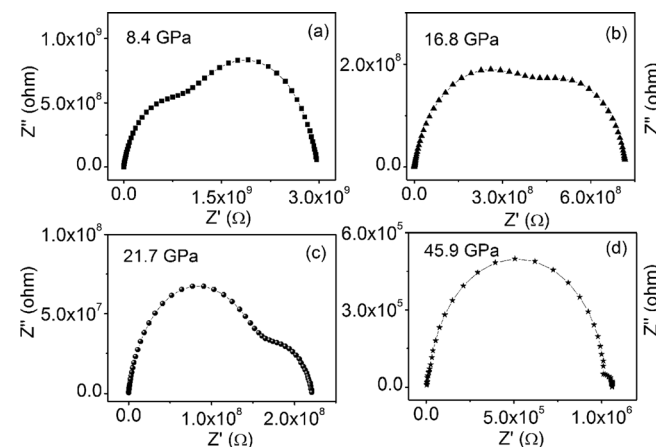


FIG. 3. Selected Nyquist diagram at various pressures. (a) At 8.4 GPa , (b) at 16.8 GPa , (c) at 21.7 GPa , and (d) at 45.9 GPa .

data are found on the right side of the plots and the higher frequency ones are on the left. In general, the electrical response from the grain boundary is associated with larger resistance and capacitance than those of the grains,^{20,21} and thus its response frequency is much lower than that of the grains.²² Therefore, the arc in Fig. 3 corresponding to high frequency on the left is considered to be due to the conduction process from the grain interior, and the one at lower frequency on the right results from the grain boundary. Largely accepted for powder samples, the equivalent circuit method is a reliable approach to describe the impedance spectra.²³ An equivalent circuit of B_{12}As_2 (Fig. 4 inset) utilized in the spectral analysis consists of two RC subcircuits in series, each of which is, respectively, attributed to the grain and grain boundary contributions. The capacitors are represented by constant phase elements (CPEs) with their impedance given by $Z_{\text{CPE}} = B^{-1}(\omega)^{-n}$, where B is a constant that is independent of frequency. The simulation of the impedance spectra at 22.9 GPa based on the equivalent circuit, as an example, is given in Fig. 4. The high correlation indicates that the proposed equivalent circuit accurately reflects the experimental data.

To further analyze the role of grain boundary in the electrical transport properties, a representation of the imaginary part of the impedance as a function of frequency was given. The purpose was to evaluate the relaxation frequency of the most resistive contribution in the imaginary part, which is related to the type and strength of the electrical relaxation phenomenon in the material.²⁴ Figure 5 shows the representative impedance spectra of the imaginary part with frequencies at selected 8.4, 16.8, 21.7, and 45.9 GPa. Two relaxation peaks can be observed in all spectra obtained in the measurements. These peaks shift toward higher frequencies with increasing pressure. The peak corresponding to the grain boundary is intense in the lower pressure range but becomes weakened upon pressure elevation in comparison to that of the grain. This implies that the grain dominantly determines the impedance at high pressures and the grain boundary effect diminishes during compression.

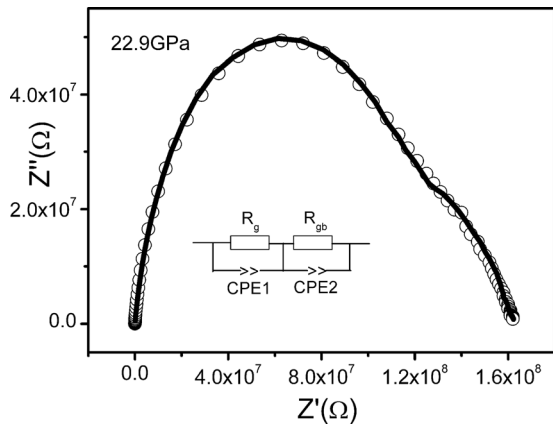


FIG. 4. Simulation of the impedance spectra at 22.9 GPa by the series R-C equivalent circuit shown in the inset. Solid circles are experimental data and the solid line is the fitted curve based on the equivalent circuit.

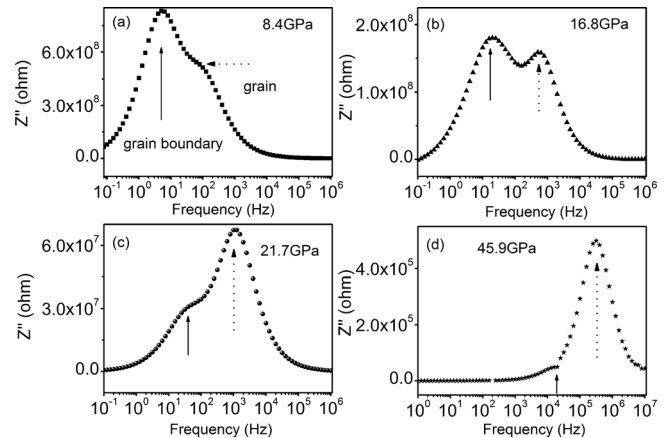


FIG. 5. Variation of the imaginary part of impedance (Z'') as a function of frequency at 8.4, 16.8, 21.7, and 45.9 GPa. The dotted and solid arrows represent the grain and grain boundary part, respectively.

The relaxation frequency of the grain and grain boundary (Fig. 6(a)) can be expressed according to the Arrhenius relationship

$$d(\ln f)/dP = -(1/k_B T)(dE_a/dP), \quad (1)$$

where E_a represents activation energy of the grain (grain boundary), k_B is the Boltzmann constant, and T is the temperature. Differentiation of the changing rates of the activation energies with pressure are shown in Fig. 6(b). For the grain, the dE_a/dP has a fluctuation when the pressure is above 6.7 GPa (while for the grain boundary, the fluctuation exists in the entire experimental pressure range). Taking the resolution of the equipment into account, it can be considered that the dE_a/dP does not change with pressure; that is,

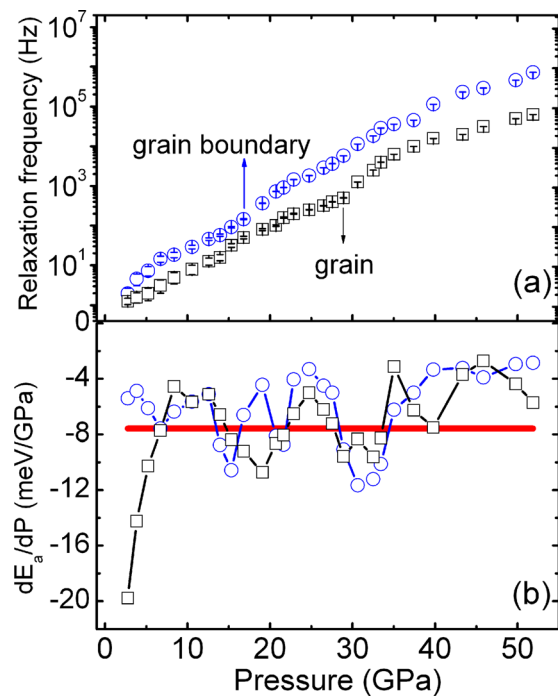


FIG. 6. (a) Pressure dependence of f_g and f_{gb} and (b) the variation of dE_a/dP with pressure. The square and circle correspond to the grain and the grain boundary, respectively.

the relationship between the activation energy and pressure is linear. By linear fitting to the curve $\ln \rho \sim P$, the pressure dependence of the activation energy is calculated to be -6.7 meV/GPa and -6.1 meV/GPa for the grain and grain boundary, respectively. Both grain and grain boundary activation energies decrease with increasing pressure in the pressure range, indicating that pressure promotes electrical conductivity.

The grain boundary properties strongly depend on the grain boundary microstructure and character, which is defined by the misorientation between adjacent grains, the grain boundary defects, and other factors.²⁵ It is known that the grain boundary impedance is caused by the depletion of charge carriers in the space charge layers adjacent to the grain boundary cores.²⁶ Using the “diffusion theory model” for a Schottky-type depletion space charge layer,²⁷ the space charge potential Φ can be calculated by the expression

$$\frac{\rho_{gb}}{\rho_g} = \frac{\exp(e\Phi/k_B T)}{2e\Phi/k_B T}, \quad (2)$$

where ρ_{gb} and ρ_g are the resistivities of the grain boundary and the grain, respectively; k_B and e denote the Boltzmann constant and the elementary charge, respectively; $T = 300 \text{ K}$. Deriving ρ_{gb} and ρ_g from the impedance measurements and the sample geometry, the pressure dependence of the space charge potential is obtained (Fig. 7).

The space charge potential changes from positive to negative at 20.7 GPa , which means $\rho_g > 2\rho_{gb}$ at higher pressures according to Eq. (2). This indicates once more that the contribution of the grain boundaries to the total resistance becomes smaller. The small contribution of grain boundaries with increasing pressure in B_{12}As_2 can be explained using the double-Schottky barrier model (Fig. 8): due to the lattice disorder and the deviation from stoichiometry in the grain boundaries, there exist many defect energy levels in the grain boundaries, such as the charge trap energy levels (e.g., the vacancy and the entangled state energy levels), which may capture many more holes from the grains with increasing pressure. This leads to carrier concentration reduction in the grains and accumulation in the grain boundaries, resulting in a relatively smaller contribution of the boundaries to the total resistance.

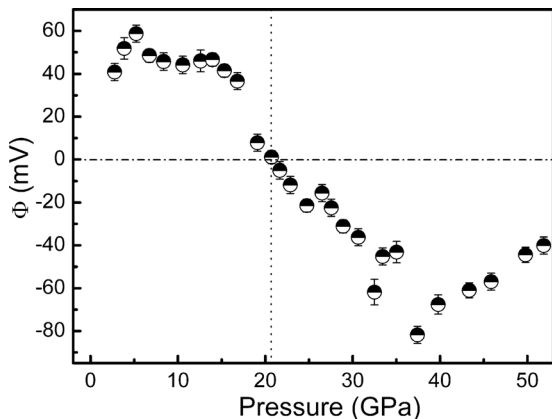


FIG. 7. The pressure dependence of space charge potential.

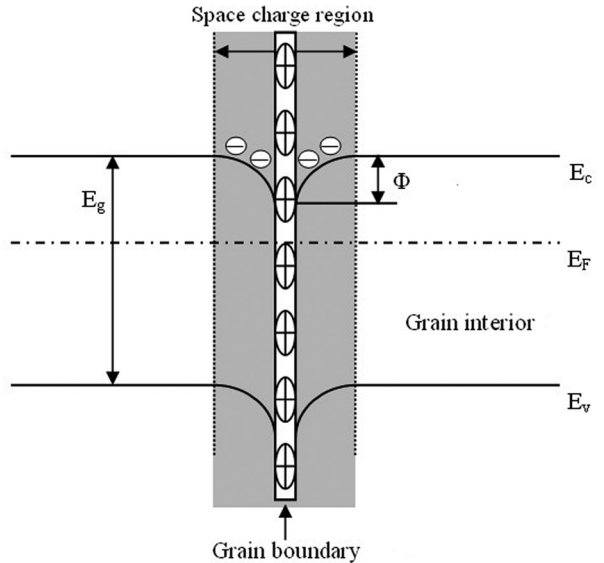


FIG. 8. Schematic of the double-Schottky barrier model near the grain boundary region. $\Phi = \varphi(g) - \varphi(gb)$ is the potential difference between grain interior (g) and grain boundary (gb).

The distribution of the cation defect concentration (N_c) and the anion defect concentration (N_a) in the grain boundary (gb) space charge layer can be expressed as^{28,29}

$$N_c(gb) = \exp\left[-\frac{F_c - Ze\varphi(gb)}{k_B T}\right], \quad (3)$$

$$N_a(gb) = \exp\left[-\frac{F_a + Ze\varphi(gb)}{k_B T}\right], \quad (4)$$

where Z is the effective charge number, F_c and F_a are the free energy of formation of the cation and anion defects.

In the grain interior (g), the crystal is electrically neutral, i.e.

$$N_c(g) = N_a(g). \quad (5)$$

Thus, we get

$$Ze\varphi(g) = (F_c - F_a)/2. \quad (6)$$

Below 20.7 GPa , Φ is positive (Fig. 7), so $F_c > F_a$ and $N_c(gb) < N_c(g)$, which indicates that the formation of anion defects is more favorable than that of cation defects. Thus, the cation defect concentration in the space-charge layer is lower than that in the grain interior. Above 20.7 GPa , Φ becomes negative, so the formation of anion defects is more difficult than that of cation defects, and the cation defect concentration in the space-charge layer is higher than that in the grain interior. This indicates that there exists a pressure-induced inversion of charge defect concentration in the space charge layer at 20.7 GPa for B_{12}As_2 .

The resistances of the grain and grain boundary are shown in Fig. 9(a). Both R_g and R_{gb} decrease with increasing pressure, indicating that compression reduces the band gap of B_{12}As_2 . The fraction of R_{gb} to the entire resistance, $R_{gb}/(R_g + R_{gb})$, also dropped with pressure elevation (Fig. 9(b)). The resistance due to the grain boundary becomes much smaller above 16.8 GPa ,

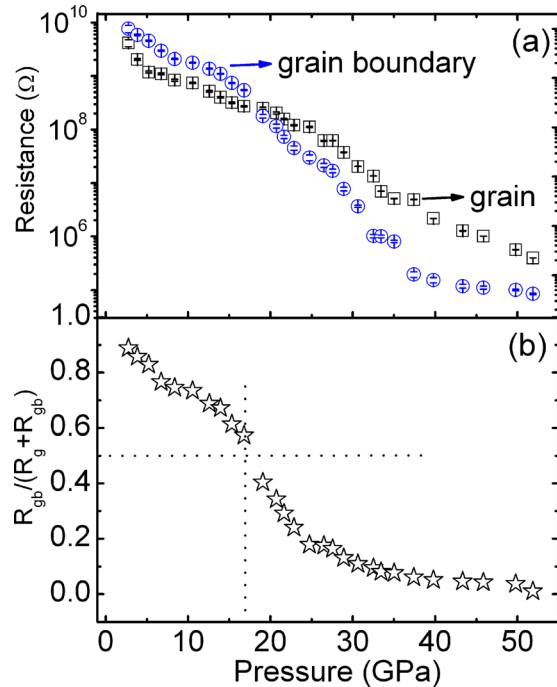


FIG. 9. (a) Pressure dependence of R_g and R_{gb} and (b) the grain boundary contribution to the total resistance.

which is also reflected in the arc in the Nyquist plots in Fig. 3. The reduction of the vacancies in the grain boundary is believed to account for such a phenomenon.

The pressure dependence of resistivity at room temperature is shown in Fig. 10. Below 22.9 GPa, the resistivity of the sample is too large and beyond the DC instrument range. As observed in Fig. 10, the resistivity decreased with increasing pressure and no abnormal change was detected in the whole pressure range, which is consistent with the fact that no structural phase transition occurs in this pressure range.^{8,9,30} In the inset of Fig. 10, the temperature dependence of the resistivity of $B_{12}As_2$ at different pressures are plotted in Arrhenius format. It can be seen that the resistivity decreases with increasing temperature and therefore $B_{12}As_2$ shows semiconductor behavior.³¹ From the temperature

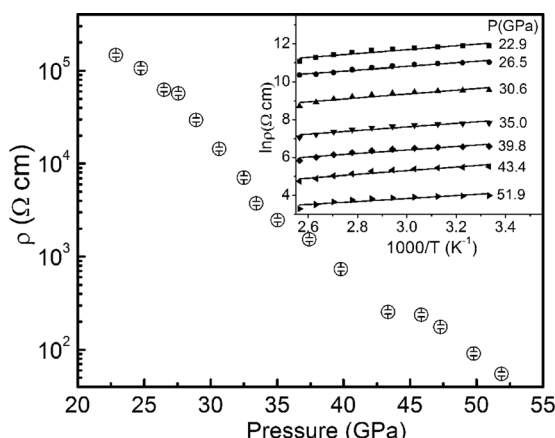


FIG. 10. Pressure dependence of the electrical resistivity of $B_{12}As_2$ at room temperature. The inset figure shows the temperature dependent resistivity under different pressures in Arrhenius format.

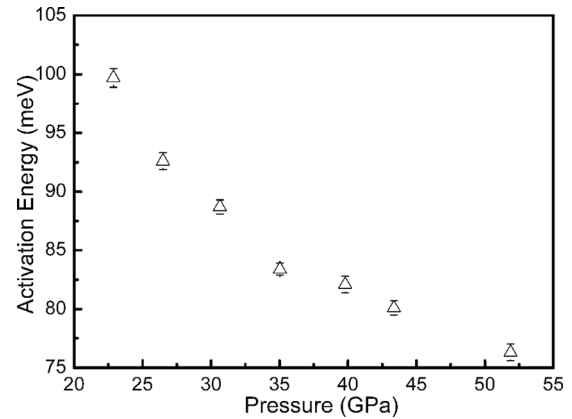


FIG. 11. Transport activation energy as a function of pressure.

dependence of resistivity, the transport activation energy (E_t) of $B_{12}As_2$ at a given pressure can be obtained according to the equation

$$\rho = \rho_0 \exp(-E_t/2k_B T), \quad (7)$$

where ρ_0 is a constant, k_B is the Boltzmann's constant, and T is the temperature. The value of E_t can be obtained by linearly fitting the plot of $\ln \rho$ versus $1000/T$. As shown in Fig. 11, E_t keeps decreasing in the pressure range. Several theoretical and experimental studies have been published on the band structure of $B_{12}As_2$, for which the band gap was reported as indirect in the range of 2.30–3.47 eV.^{32–36} It is obvious that the value of E_t is much less than that of the band gap and thus E_t is determined by defect energy levels in the band gap. A linear extrapolation of the transport activation energy predicts E_t going to zero around 150 GPa, that is, the $B_{12}As_2$ would become metallic above 150 GPa. Further study on this prediction is needed. As mentioned above, the grain boundary resistance becomes relatively much smaller above 16.8 GPa and, then, the grain boundary activation energy becomes lower than that of the grain, so E_t is related to the defect in the grain interior.

IV. CONCLUSION

In summary, we performed *in situ* high-pressure impedance spectroscopy and high-temperature resistivity measurements of polycrystalline $B_{12}As_2$. The analysis has established that both the grain and grain boundary resistance smoothly decrease with increasing pressure. The pressure dependence of the space charge potential was obtained from the double-Schottky barrier model. The contribution of the grain boundaries to the total resistance becomes smaller at higher pressure and a pressure-induced inversion of charge defect concentration in the space charge layer was found at 20.7 GPa. By high temperature resistivity measurements, the transport activation energy under pressure was obtained.

ACKNOWLEDGMENTS

Thanks are due to Dr. James Edgar, Kansas State University for synthesizing and providing samples for the

experiments. The research was supported by the National Science Foundation (Grant No. DMR-1435170), the National Basic Research Program of China (Grant No. 2011CB808204), the National Natural Science Foundation of China (Grant Nos. 11374121, 11404133, and 11304034), China Postdoctoral Science Foundation (Grant No. 2013M540243), and Program of Science and Technology Development Plan of Jilin Province (Grant Nos. 20140520105JH and 201201106).

- ¹D. Emin, *Phys. Today* **40**(1), 55 (1987).
- ²V. V. Brazhkin, A. G. Lyapin, and R. J. Hemley, *Philos. Mag. A* **82**, 231 (2002).
- ³A. Masago, K. Shirai, and H. Katayama-Yoshida, *Phys. Rev. B* **73**, 104102 (2006).
- ⁴N. Vast, S. Baroni, G. Zerah, J. Besson, A. Polian, M. Grimsditch, and J. Chervin, *Phys. Rev. Lett.* **78**, 693 (1997).
- ⁵J. Nagamatsu, N. Nakagawa, T. Muranaka, Y. Zenitani, and J. Akimitsu, *Nature* **410**, 63 (2001).
- ⁶D. Emin, *J. Solid State Chem.* **179**, 2791 (2006).
- ⁷M. Carrard, D. Emin, and L. Zuppiroli, *Phys. Rev. B* **51**, 11270 (1995).
- ⁸S. V. Ovsyannikov, A. Polian, P. Munsch, J.-C. Chervin, G. Le Marchand, and T. L. Aselage, *Phys. Rev. B* **81**, 140103(R) (2010).
- ⁹J. Wu, H. Zhu, D. Hou, C. Ji, C. Whiteley, J. Edgar, and Y. Ma, *J. Phys. Chem. Solids* **72**, 144 (2011).
- ¹⁰T. Chu and A. Hyslop, *J. Electrochem. Soc.* **121**, 412 (1974).
- ¹¹S. Bakalova, Y. Gong, C. Cobet, N. Esser, Y. Zhang, J. Edgar, M. Dudley, and M. Kuball, *Phys. Rev. B* **81**, 075114 (2010).
- ¹²T. Watanabe, M. Yamada, and S. Karashima, *Philos. Mag. A* **63**, 1013 (1991).
- ¹³H. Yoshida, T. Yamamoto, Y. Ikuhara, and T. Sakuma, *Philos. Mag. A* **82**, 511 (2002).
- ¹⁴H. Y. Chang, S. Y. Cheng, and C. I. Sheu, *Acta Mater.* **52**, 5389 (2004).
- ¹⁵Y. Han, C. Gao, Y. Ma, H. Liu, Y. Pan, J. Luo, M. Li, C. He, X. Huang, and G. Zou, *Appl. Phys. Lett.* **86**, 064104 (2005).
- ¹⁶C. Whiteley, Y. Zhang, Y. Gong, S. Bakalova, A. Mayo, J. Edgar, and M. Kuball, *J. Cryst. Growth* **318**, 553 (2011).
- ¹⁷M. Li, C. Gao, G. Peng, C. He, A. Hao, X. Huang, D. Zhang, C. Yu, Y. Ma, and G. Zou, *Rev. Sci. Instrum.* **78**, 075106 (2007).
- ¹⁸B. Liu, Y. Han, C. Gao, Y. Ma, G. Peng, B. Wu, C. Liu, Y. Wang, T. Hu, and X. Cui, *J. Phys. Chem. C* **114**, 14251 (2010).
- ¹⁹H. Mao, J.-A. Xu, and P. Bell, *J. Geophys. Res.: Solid Earth* **91**, 4673 (1986).
- ²⁰D. C. Sinclair, T. B. Adams, F. D. Morrison, and A. R. West, *Appl. Phys. Lett.* **80**, 2153 (2002).
- ²¹D. C. Sinclair and A. R. West, *J. Appl. Phys.* **66**, 3850 (1989).
- ²²J. Liu, C.-G. Duan, W.-N. Mei, R. W. Smith, and J. R. Hardy, *J. Appl. Phys.* **98**, 093703 (2005).
- ²³D. Zhang, Y. Zhang, Y. Gao, Y. Han, C. Gao, Y. Ma, C. Cheng, and K. Yu, *J. Appl. Phys.* **111**, 063718 (2012).
- ²⁴S. Dutta, R. Choudhary, P. Sinha, and A. K. Thakur, *J. Appl. Phys.* **96**, 1607 (2004).
- ²⁵T. Watanabe, *J. Mater. Sci.* **46**, 4095 (2011).
- ²⁶B. D. Huey and D. A. Bonnell, *Solid State Ionics* **131**, 51 (2000).
- ²⁷H. K. Henisch, *Semiconductor Contacts* (Clarendon Press, Oxford, U.K., 1984), p. 45.
- ²⁸K. Kliewer and J. Koehler, *Phys. Rev.* **140**, A1226 (1965).
- ²⁹X. Guo, *Solid State Ionics* **81**, 235 (1995).
- ³⁰J. Pomeroy, M. Kuball, H. Hubel, N. Van Uden, D. Dunstan, R. Nagarajan, and J. Edgar, *J. Appl. Phys.* **96**, 910 (2004).
- ³¹G. Itkin, G. R. Hearne, E. Sterer, M. P. Pasternak, and W. Potzel, *Phys. Rev. B* **51**, 3195 (1995).
- ³²D. Li and W. Y. Ching, *Phys. Rev. B* **52**, 17073 (1995).
- ³³D. R. Armstrong, J. Bolland, and P. G. Perkins, *Theor. Chim. Acta* **64**, 501 (1984).
- ³⁴I. Morrison, D. M. Bylander, and L. Kleinman, *Phys. Rev. B* **45**, 1533 (1992).
- ³⁵F. Gao, X. Qin, L. Wang, Y. He, G. Sun, L. Hou, and W. Wang, *J. Phys. Chem. B* **109**, 14892 (2005).
- ³⁶G. A. Slack, T. McNelly, and E. Taft, *J. Phys. Chem. Solids* **44**, 1009 (1983).